

## X-ray photoelectron spectra, theoretical band structures, and densities of states for BaTiO<sub>3</sub> and KNbO<sub>3</sub>

P. Pertosa

*Institut de Physique Nucléaire (et IN2P3), Université Lyon-1 43, Bd du 11 Novembre 1918-69621 Villeurbanne, France*

F. M. Michel-Calendini

*Laboratoire d'Electronique et Physique des Solides, Université Lyon-1  
43, Bd du 11 Novembre 1918-69621 Villeurbanne, France*

(Received 19 July 1977)

X-ray photoelectron spectra of the valence bands and core levels for electron binding energies ranging from 0 to 45 eV, are presented for the two perovskite-type compounds BaTiO<sub>3</sub> and KNbO<sub>3</sub>. Theoretical band structures and densities of states are calculated using a parametrized tight-binding method. The validity of the comparison between theoretical results and experimental valence-band spectra is discussed. The effects of the various interatomic interaction matrix elements are analyzed and theoretical results are also presented for SrTiO<sub>3</sub> in order to compare this work to earlier calculations. Photoionization cross sections are introduced in the densities-of-states computations: their contribution in modulating the valence-band shape is much more significant for KNbO<sub>3</sub> than for BaTiO<sub>3</sub>. The present densities of states seem to reproduce in an adequate way the main structures of the experimental valence-band spectra.

### I. INTRODUCTION

Among the various experimental methods providing information on the electronic levels in a solid material, x-ray photoelectron spectroscopy (XPS) seems to give the best insight in the energy distribution  $\rho(E)$  of occupied electronic states. Due to the final hole state, various effects such as relaxation, multiplet splitting, or shake-up excitations may induce perturbations compared to the initial ground state, but it often occurs that XPS spectra reflect the actual density of occupied states, modulated by photoionization cross sections. In such cases, band-structure calculations can be correlated in a direct way to experimental valence-band spectra.

Earlier XPS measurements on perovskite type compounds have been obtained by Board,<sup>1</sup> Kowalczyk,<sup>2</sup> and Battye *et al.*<sup>3</sup> for SrTiO<sub>3</sub> and BaTiO<sub>3</sub> ceramic. Several band-structure computations have also been performed on ABO<sub>3</sub> perovskites. The pioneering work of Khan and Leyendecker<sup>4</sup> on SrTiO<sub>3</sub> was followed by the complete APW tight-binding calculation of Mattheiss<sup>5</sup>; Soules *et al.*<sup>6</sup> used a self-consistent tight-binding computation with an extended basis set of 34 atomic orbitals to determine the electronic levels of SrTiO<sub>3</sub>. The BaTiO<sub>3</sub> band structures in cubic and tetragonal phases have been given by Michel-Calendini and Mesnard<sup>7,8</sup> with a restricted basis set of 14 atomic orbitals and semiempirical parameters for off-diagonal integrals. Recently, Battye *et al.*<sup>3</sup> have compared SrTiO<sub>3</sub> and BaTiO<sub>3</sub> valence-band spectra with existing theoretical predictions and concluded that the agreement was not satisfying.

The aim of the present work is to compare XPS measurements on single crystals of BaTiO<sub>3</sub> and KNbO<sub>3</sub> to the density-of-states histograms deduced from electronic levels, when the inner orbital interactions and the photoionization cross sections are included in the computation.

Experimental valence-band spectra and core level binding energies are given in Sec. II. The outline of computations and band structures for cubic BaTiO<sub>3</sub>, KNbO<sub>3</sub>, and SrTiO<sub>3</sub> are reported in Sec. III. The influence of inner orbital interactions and photoionization cross sections are discussed in Sec. IV. The general discussion of our results is presented in Sec. V.

### II. XPS MEASUREMENTS

XPS spectra were obtained using a Hewlett-Packard 5950A spectrometer. The incident x-ray is the monochromatized Al K $\alpha$  radiation. The total instrumental resolution is estimated to be 0.55 eV as measured on the Fermi level of gold. BaTiO<sub>3</sub> and KNbO<sub>3</sub> samples are transparent colorless single crystals: BaTiO<sub>3</sub> is cut from a commercially available sample grown using the method described by Linz,<sup>9</sup> while KNbO<sub>3</sub> is obtained by a new method of growth by Metrat.<sup>10</sup> At room temperature, BaTiO<sub>3</sub> is in the tetragonal phase and KNbO<sub>3</sub> in the orthorhombic phase. The various spectra do not exhibit photopeaks of any impurity. The valence bands (hereafter denoted VB) and core levels for BaTiO<sub>3</sub> and KNbO<sub>3</sub> are reported on Fig. 1 for binding energies from 0 to 45 eV below the valence-band edge.

The main problem is to obtain clean sample

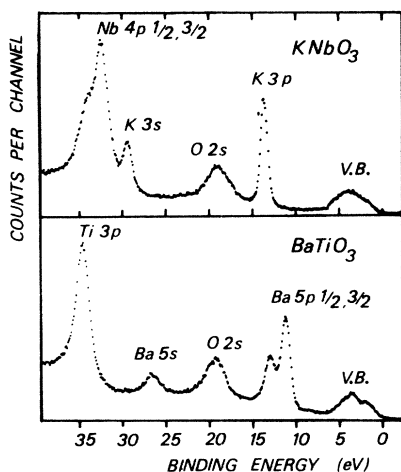


FIG. 1. XPS spectra of  $\text{KNbO}_3$  and  $\text{BaTiO}_3$  for electron binding energies ranging from 0 to 45 eV.

surfaces. The treatment which gives the minimum carbon pollution is scraping of the surface with a diamond grinding tool followed by an ultrasonic washing in ethanol or methanol for a few minutes. The crystal is immediately introduced into the spectrometer chamber after drying. This preparation makes evident the actual bulk properties. On the contrary, if the scraping is made in the preparation chamber (in vacuum without ultrasonic washing), the core photopeaks of Ba ( $\text{BaTiO}_3$ ) and K ( $\text{KNbO}_3$ ) reveal several chemical states for these ions. By scraping the surface sample, we break chemical bonds and a powder is created from the crystal with a large specific surface. The different chemical states which appear for Ba and K atoms are explained, we think, by the high reactivity of these elements with oxygen even in the  $10^{-7}$ -Torr pressure of the preparation chamber. Ultrasonic cleaning eliminates this powder.

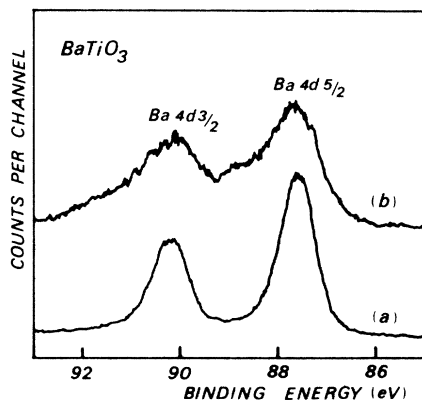


FIG. 2. Ba-4d photopeaks in  $\text{BaTiO}_3$ : (a) after the cleaning process described in the text; (b) after Ar-ion bombardment.

The same phenomenon occurs when argon ion bombardment is used for the cleaning: the effect is even more drastic depending on the  $\text{Ar}^+$  ion energy and on the intensity of the beam. We then notice changes in stoichiometry and the destruction mainly of cationic sites, as shown on Fig. 2 for the Ba 4d levels. The same effect seems to appear also in the work of Battye<sup>3</sup> where *in situ* scraping without washing is used: the Ba-5p photopeak becomes larger and the  $5p_{1/2}$ - $5p_{3/2}$  spin-orbit splitting does not appear clearly. In our case, these problems are avoided and the carbon contamination is negligible. We observe a very weak C-1s signal, but we do not distinguish any C-2s signal. To make sure of this fact, samples were observed with some more carbon and the C-2s peak appears at a higher binding energy than the O-2p valence band, as we can see on Fig. 3. We notice also a small shoulder on the high binding energy side of the O-1s signal when the sample is not scraped *in situ*, denoting the presence of adsorbed oxygen. The magnitude of this component is about 10% of the bulk O-1s signal and the percentage of oxygen adsorbate does not induce observable variations, in the VB spectra.<sup>3</sup>

In short, it seems difficult to obtain at the same time samples without oxygen adsorption or carbon contamination which display only the bulk chemical states for Ba or K atoms. The best method would be to cleave the crystals *in situ*, but the present preparation is believed to be sufficiently indicative of the bulk properties to allow meaningful comparison of XPS experiments with theory.

After cleaning, samples were introduced into the spectrometer chamber where the pressure is about  $6 \times 10^{-9}$  Torr at the beginning of scanning. The pressure decreases then to  $10^{-9}$  Torr after some hours and the C-1s signal does not increase dur-

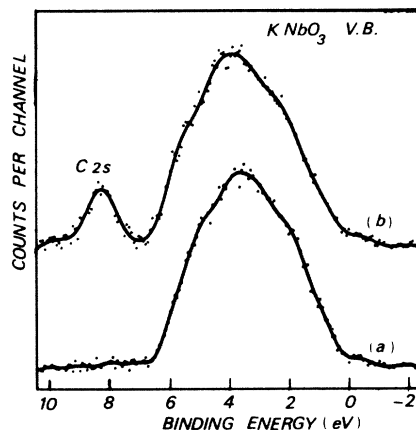


FIG. 3. XPS spectra of the  $\text{KNbO}_3$  valence band: (a) without carbon pollution; (b) the C-2s photopeak appears at a binding energy of 8 eV below the valence-band

ing the experiment.

Both samples give charging effects under x-ray irradiation. This effect was estimated to be about 1 eV for  $\text{KNbO}_3$  and 10–15 eV for  $\text{BaTiO}_3$  samples. In our case, absolute electronic binding energies are not necessary because the valence-band edge is a suitable reference for comparison with theoretical densities of states. However, inhomogeneous charging often tends to broaden the photopeaks and affects the resolution, so we used a flood gun with a low current of thermal energy electrons to prevent the charging. The O-1s line is fixed at 531.0 eV, and the relative core level binding energies are reported in Table I.

### III. BAND STRUCTURE OF $ABO_3$ CRYSTALS IN THE CUBIC PHASE

The crystal unit cell and related Brillouin zone of cubic  $ABO_3$  perovskites are shown in Fig. 4. Energy levels  $E_n(\vec{k})$  vs  $\vec{k}$  wave vector are determined according to the tight-binding method already described for  $\text{BaTiO}_3$ .<sup>7,8</sup> The atomic basis set includes the  $ms$ ,  $mp$ , and  $md$  orbitals of the  $B$  ion ( $m=3$  for Ti,  $m=4$  for Nb), the  $ns$  and  $np$  orbitals of the  $A$  ion ( $n=3, 4,$  and  $5$  for K, Sr, and Ba), and the  $2s$  and  $2p$  orbitals of oxygen. The linear combination of atomic orbitals (LCAO) wave function  $\Phi_{n\vec{k}}$  relative to  $E_n(\vec{k})$  is of the form

$$\Phi_{n\vec{k}} = \sum_{\mu, i} D_{n\mu i} \chi_{\mu i\vec{k}}(\vec{r}) \quad (1)$$

with

$$\chi_{\mu i\vec{k}}(\vec{r}) = N^{-1/2} \sum_q \chi_i(\vec{r} - \vec{R}_q - \vec{r}_\mu) e^{i\vec{k} \cdot (\vec{R}_q + \vec{r}_\mu)},$$

TABLE I. XPS determination of core level binding energies relative to the O-1s level taken at 531.0 eV for  $\text{KNbO}_3$  and  $\text{BaTiO}_3$ .

Level	$\text{KNbO}_3$ Binding energy (eV)	Level	$\text{BaTiO}_3$ Binding energy (eV)
O 1s	531.00	O 1s	531.00
Nb 3d <sub>3/2</sub>	210.9 (±0.1)	Ti 2p <sub>1/2</sub>	465.6 (±0.1)
Nb 3d <sub>5/2</sub>	208.1 (±0.1)	Ti 2p <sub>3/2</sub>	459.8 (±0.1)
K 2p <sub>1/2</sub>	295.6 (±0.1)	Ba 4d <sub>3/2</sub>	92.5 (±0.1)
K 2p <sub>3/2</sub>	292.8 (±0.1)	Ba 4d <sub>5/2</sub>	89.8 (±0.1)
Nb 4p <sub>1/2</sub>	38.0 (±0.1)	Ti 3p <sub>1/2</sub>	38.6 (±0.1)
Nb 4p <sub>3/2</sub>	36.3 (±0.1)	Ti 3p <sub>3/2</sub>	
K 3s	33.4 (±0.1)	Ba 5s	30.5 (±0.1)
O 2s	22.8 (±0.1)	O 2s	23.0 (±0.1)
K 3p <sub>1/2</sub>	17.3 (±0.1)	Ba 5p <sub>1/2</sub>	16.7 (±0.1)
K 3p <sub>3/2</sub>		Ba 5p <sub>3/2</sub>	14.9 (±0.1)

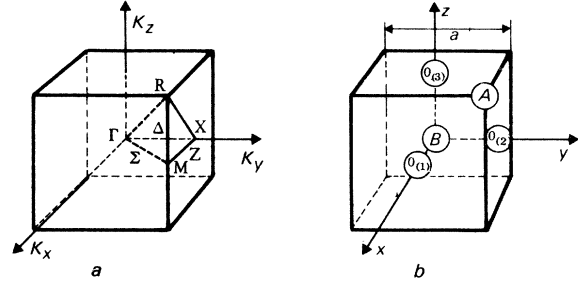


FIG. 4. (a) First Brillouin zone for cubic  $ABO_3$  structure; (b) Unit cell for cubic  $ABO_3$  structure. The atomic positions are the following:  $\vec{r}_B=0$ ,  $\vec{r}_{O(i)}=d_{BO(i)}\vec{a}_i$ , and  $\vec{r}_A=\vec{a}_1+\vec{a}_2+\vec{a}_3$ , with  $|\vec{a}_i|=\frac{1}{2}a$ .

where  $\chi_i(\vec{r} - \vec{R}_q - \vec{r}_\mu)$  is the atomic orbital of symmetry  $i$  localized at the  $\mu$  site in the  $q$  unit cell.

Diatomic overlap  $S_{ij}$  and kinetic energy terms  $T_{ij}$  are exactly computed for first and second nearest neighbors of  $A$ - $B$ ,  $A$ - $A$ ,  $A$ - $O$ ,  $B$ - $B$ ,  $B$ - $O$ , and  $O$ - $O$  interactions. Diagonal terms of the Hamiltonian matrix  $H_i^\mu$  are approximated as a sum of a mono-electronic energy  $E_i^\mu$  and a Madelung energy  $E_{\text{Mad}}^\mu$ , which are functions of the ionic charges  $q_\mu$  at the  $\mu$  sites.

For the central atom  $B$ , the charge dependence of  $E_i^\mu$  is obtained by a quadratic interpolation of the form

$$E_i^\mu = A_i^\mu q_\mu^2 + B_i^\mu q_\mu + C_i^\mu, \quad (2)$$

where the  $A$ ,  $B$ , and  $C$  coefficients are determined from the mono-electronic energies of  $\text{Ti}^{q+}$  and  $\text{Nb}^{q+}$  given by Clementi<sup>11</sup> and Richardson<sup>12</sup> with  $q$  varying from 1 to 3. For oxygen, the  $E_i^O$  are obtained from an interpolated relation on electron affinities of  $\text{O}^-$  and  $\text{O}^{2-}$  and from Moore's data tables.<sup>13</sup>

The  $E_{3s}^K$  and  $E_{3p}^K$  are deduced from Basch's tables.<sup>14</sup> We assume the charge is 2 on Sr and Ba ions and take  $E_{4p}^{\text{Sr}}$ ,  $E_{5p}^{\text{Ba}}$  to be the experimental ionization potentials of  $\text{Sr}^{2+}$  and  $\text{Ba}^{2+}$ . The  $E_{4s}^{\text{Sr}}$ ,  $E_{5s}^{\text{Ba}}$  are obtained from the preceding values by

$$E_{ms}^A - E_{mp}^A = \Delta\epsilon^A, \quad (3)$$

where  $\Delta\epsilon^A$  is the difference between the mono-electronic energies  $\epsilon_{ms}$  and  $\epsilon_{mp}$  of neutral Ba and Sr given by Herman's and Skillman's tables,<sup>15</sup> whose results are in accord with Mann's tables<sup>16</sup> for these atoms. The Madelung potentials  $V_{\text{Mad}}^\mu$  at  $A$ ,  $B$ , and  $O$  sites are computed by the Van Gool and Piken program.<sup>17</sup> Off-diagonal diatomic transfer integrals  $H_{ij}^{\mu\nu}$  can be approximated using several semiempirical relations. The first one, used for  $\text{BaTiO}_3$ ,<sup>7,8</sup> was the Wolfsberg-Helmholz method.<sup>18</sup> The other, already described by Jacquier<sup>19</sup> for cluster computations, is of the form

$$H_{ij}^{\mu\mu'} = \frac{1}{2} F_{ij}^{\mu\mu'} S_{ij}^{\mu\mu'} \times \left( E_i^\mu + E_j^{\mu'} + H_i^\mu + H_j^{\mu'} + \frac{q_\mu + q_{\mu'}}{r_{\mu\mu'}} \right) - T_{ij}^{\mu\mu'}, \quad (4)$$

where  $F_{ij}^{\mu\mu'}$  is taken to be unity. The charges  $q_\mu$  and  $q_{\mu'}$  are deduced from a Mulliken population analysis,<sup>20</sup>  $T_{ij}^{\mu\mu'}$  is the kinetic energy term and  $r_{\mu\mu'} = |\vec{r}_\mu - \vec{r}_{\mu'}|$ . Relation (4) receives more theoretical justification than the Wolfsberg-Helmholz scheme. However, it appears difficult to obtain results in agreement in the same time with band-gap values, optical spectra, and XPS valence bands when the self-consistency among the charges is reached. So in the present computations for BaTiO<sub>3</sub> and KNbO<sub>3</sub>, instead of testing the calculated ionic charges which are strongly dependent on the spatial extension of the radial wave functions, we adjusted the  $q_\mu$  charges and varied the  $F_{ij}$  parameters from 0.4 to 1 to reliably fit the 2*p*-3*d* band gap, the calculated density of states (hereafter denoted DOS), and the optical spectra to experiment.<sup>21</sup>

The SrTiO<sub>3</sub> band structure presented in this work is based upon the adjusted APW tight-bind-

ing computation of Mattheiss<sup>5</sup> with modified overlap matrix elements  $S_{ij}$  determined as for BaTiO<sub>3</sub>. To compare the inner states of Sr and Ti ions to the  $\epsilon_{3d}^{Ti}$  parameter of Mattheiss, we have first determined  $H_i^{Ti}$  and  $H_i^{Sr}$  by relations (2) and (3) for Sr<sup>2+</sup>Ti<sup>3+</sup>O<sup>5/3-</sup>, including the Madelung terms. Then the  $E_i^\mu$  and  $H_i^\mu$  parameters used in our computations are related to  $\epsilon_{3d}^{Ti}$  by

$$H_i^\mu = \epsilon_{3d}^{Ti} - H_{3d}^{Ti} + H_i^{\mu}$$

and

$$E_i^\mu = H_i^\mu - E_{Mad}^\mu.$$

Off-diagonal terms Sr-Sr, Ti-Ti are estimated by relation (4), and Sr-O, Sr-Ti interactions are neglected.

Radial wave functions used in this work are taken from Clementi's tables<sup>11</sup> for Ti<sup>3+</sup> and K<sup>+</sup>, from Watson<sup>22</sup> for O<sup>2-</sup>, from Clementi, Raimondi, and Reinhard<sup>23</sup> for Ba and Sr and from Richardson's data<sup>12</sup> for Nb<sup>3+</sup>.

The values of  $S_{ij}^{\mu\mu'}$  and  $H_{ij}^{\mu\mu'}$  matrix elements are given in Table II, under the label  $E_{ij}(\alpha, \beta, \gamma)$ , where  $(\alpha, \beta, \gamma)$  stand for the coordinates of  $\vec{r}_\mu - \vec{r}_{\mu'}$ . For convenience, general parameter

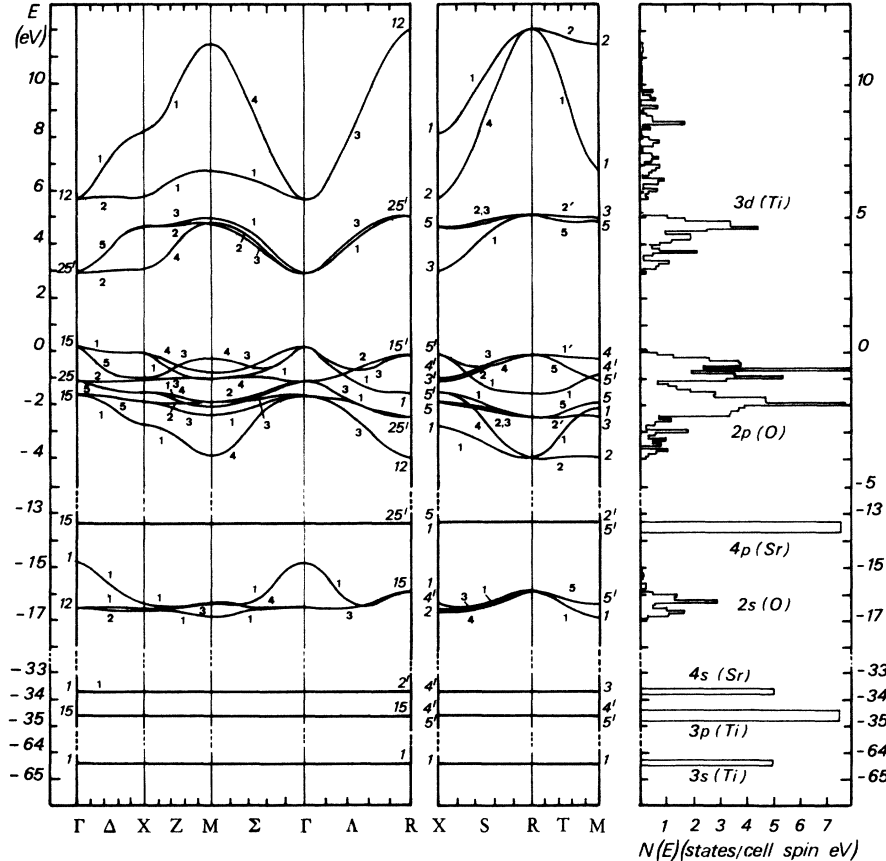


FIG. 5. Band-structure results and density of states (on the right-hand side) for SrTiO<sub>3</sub>.

TABLE II. Diatomic overlap  $S_{m,n}(\alpha, \beta, \gamma)$  and transfer integrals  $H_{m,n}(\alpha, \beta, \gamma)$  (in eV) for BaTiO<sub>3</sub>, KNbO<sub>3</sub>, and SrTiO<sub>3</sub>.

Two-center approximation			BaTiO <sub>3</sub> ( $a = 4.000 \text{ \AA}$ )		KNbO <sub>3</sub> ( $a = 3.997 \text{ \AA}$ )		SrTiO <sub>3</sub> ( $a = 3.900 \text{ \AA}$ )		
Interaction	$D_i$	$E_{i,j}(\alpha, \beta, \gamma)$	$S_{m,n}(\alpha, \beta, \gamma)$	$H_{m,n}(\alpha, \beta, \gamma)$	$S_{m,n}(\alpha, \beta, \gamma)$	$H_{m,n}(\alpha, \beta, \gamma)$	$S_{m,n}(\alpha, \beta, \gamma)$	$H_{m,n}(\alpha, \beta, \gamma)$	
B-B	$D_1$	$E_{s,s}(0, 0, 0)$	1.0	-75.1842	1.0	-71.1430	1.0	-64.3791	
	$D_2$	$E_{x,x}(0, 0, 0)$	1.0	-45.5022	1.0	-45.1067	1.0	-34.6318	
	$D_3$	$E_{x,x}(1, 0, 0)$	$-1.0 \cdot 10^{-4}$	-0.0027	0				
	$D_4$	$E_{3x^2-r^2, 3x^2-r^2}(0, 0, 0)$	1.0	-7.8652	1.0	-8.9950	1.0	2.9920	
	$D_5$	$E_{xy,xy}(0, 0, 0)$	1.0	-7.8652	1.0	-8.9950	1.0	2.9920	
	$D_6$	$E_{3x^2-r^2, 3x^2-r^2}(0, 0, 1)$	0.0015	0.0193	0.0059	-0.2638			
	$D_7$	$E_{xy,xy}(1, 0, 0)$	$3.0 \cdot 10^{-4}$	0.0082	0.0017	-0.0680			
O-O	$D_8$	$E_{xy,xy}(0, 0, 1)$	0	-0.0008	0.0001	-0.0054	0	-0.01632	
	$D_9$	$E_{s_1, s_1}(0, 0, 0)$	1.0	-30.0533	1.0	-31.8667	1.0	-15.8005	
	$D_{10}$	$E_{s_2, s_1}(\frac{1}{2}, \frac{1}{2}, 0)$	0.0155	-0.7099	0.0156	-0.7507	0.0175	-0.1251	
	$D_{11}$	$E_{s_1, s_1}(1, 0, 0)$	0.0010	-0.0408	0.0010	-0.0435	0	0	
	$D_{12}$	$E_{s_3, s_3}(0, 0, 0)$	1.0	-12.1203	1.0	-13.9323	1.0	-0.8119	
	$D_{13}$	$E_{x_1, x_2}(\frac{1}{2}, -\frac{1}{2}, 0)$	-0.0373	0.5930	-0.0373	0.6746	-0.0405	0.1938	
	$D_{14}$	$E_{x_1, x_1}(1, 0, 0)$	-0.0426	0.4542	-0.0426	0.5467	-0.0467	0.0381	
	$D_{15}$	$E_{y_1, y_1}(0, 0, 0)$	1.0	-12.1203	1.0	-13.9323	1.0	-0.8119	
	$D_{16}$	$E_{x_1, y_2}(\frac{1}{2}, -\frac{1}{2}, 0)$	0.0848	-1.1424	0.0849	-1.3246	0.0931	-0.2319	
	$D_{17}$	$E_{y_1, y_1}(1, 0, 0)$	0.0113	-0.1115	0.0113	-0.1361	0.0127	-0.0218	
	$D_{18}$	$E_{s_1, y_2}(\frac{1}{2}, -\frac{1}{2}, 0)$	-0.0550	1.8330	-0.0550	2.0387			
	$D_{19}$	$E_{s_1, y_1}(1, 0, 0)$	-0.0172	0.5440	-0.0172	0.5930			
A-A	$D_{20}$	$E_{s,s}(0, 0, 0)$	1.0	-36.1392	1.0	-36.7648	1.0	-33.7496	
	$D_{21}$	$E_{s,s}(1, 0, 0)$	0.0002	-0.0051	0.0012	-0.0649	0.0001	-0.0060	
	$D_{22}$	$E_{x,x}(0, 0, 0)$	1.0	-19.4845	1.0	-20.6499	1.0	-13.4118	
	$D_{23}$	$E_{x,x}(1, 0, 0)$	-0.0028	0.0508	-0.0038	0.1318	-0.0004	0.0081	
	$D_{24}$	$E_{y,y}(1, 0, 0)$	0.0002	-0.0015	0.0004	-0.0142	0.0003	-0.0005	
	$D_{25}$	$E_{s,x}(1, 0, 0)$	-0.0009	-0.0038	0	0	0	0	
	O-B	$D_{26}$	$E_{s_3, 3x^2-r^2}(0, 0, \frac{1}{2})$	0.0966	-3.6176	0.1664	-5.4291	0.1051	-2.5582
$D_{27}$		$E_{s_3, 3x^2-r^2}(0, 0, \frac{1}{2})$	0.1062	-3.7454	0.1557	-4.7203	0.1099	-2.2522	
$D_{28}$		$E_{x_2, xy}(0, \frac{1}{2}, 0)$	-0.0777	1.8795	-0.1256	2.6330	-0.0845	1.1356	
$D_{29}^*$		$E_{s_2, s}(0, 0, \frac{1}{2})$	0.0413	-3.0620	0.0491	-2.4944			
$D_{30}^*$		$E_{s_3, s}(0, 0, \frac{1}{2})$	0.1547	-5.7020	0.1625	-5.7497			
$D_{31}^*$		$E_{s_3, x}(0, 0, \frac{1}{2})$	-0.0610	3.4267					
$D_{32}^*$		$E_{s_3, x}(0, 0, \frac{1}{2})$	-0.1208	5.0698	-0.1404	5.1002			
$D_{33}^*$		$E_{x_3, x}(0, 0, \frac{1}{2})$	0.0426	-1.5636	0.0486	-1.4968			
A-O		$D_{34}^{**}$	$E_{ss_3}(\frac{1}{2}, \frac{1}{2}, 0)$	0.0152	-0.2390	0.0091	-0.1524		
		$D_{35}^{**}$	$E_{s, x_3}(\frac{1}{2}, \frac{1}{2}, 0)$	-0.0629	1.2934	-0.0432	0.9143		
		$D_{36}^{**}$	$E_{x, s_3}(\frac{1}{2}, \frac{1}{2}, 0)$	0.0226	-0.2737	0.0164	-0.2480		
	$D_{37}^{**}$	$E_{xx_3}(\frac{1}{2}, \frac{1}{2}, 0)$	-0.0417	0.6983	-0.0296	0.5205			
	$D_{38}^{**}$	$E_{x, y_3}(\frac{1}{2}, \frac{1}{2}, 0)$	-0.0684	1.0331	-0.0487	0.7854			
A-B	$D_{39}^{**}$	$E_{s, x}(\frac{1}{2}, \frac{1}{2}, \frac{1}{2})$	-0.0008	0.0100	-0.0009	0.0200			
	$D_{40}^{**}$	$E_{x, y}(\frac{1}{2}, \frac{1}{2}, \frac{1}{2})$	-0.0010	0.0100	-0.0013	0.0242			
	$D_{41}^{**}$	$E_{s, xy}(\frac{1}{2}, \frac{1}{2}, \frac{1}{2})$	0.0021	-0.0055	0.0033	-0.0407			
	$D_{42}^{**}$	$E_{x, yx}(\frac{1}{2}, \frac{1}{2}, \frac{1}{2})$	0.0039	-0.0168	0.0062	-0.0793			
	$D_{43}^{**}$	$E_{s, s}(\frac{1}{2}, \frac{1}{2}, \frac{1}{2})$	0.0002	-0.0011	0.0003	-0.0050			
	$D_{44}^{**}$	$E_{s, x}(\frac{1}{2}, \frac{1}{2}, \frac{1}{2})$	-0.0005	0.0061	-0.0004	0.0044			
	$D_{45}^{**}$	$E_{x, s}(\frac{1}{2}, \frac{1}{2}, \frac{1}{2})$	0.0006	-0.0096	0.0001	-0.0372			
	$D_{46}^{**}$	$E_{x, 3x^2-r^2}(\frac{1}{2}, \frac{1}{2}, \frac{1}{2})$	-0.0010	0.0042	-0.0021	0.0201			

labels  $D_i$  ( $i=1$  to 46) are used in further discussions. Overlap values less than  $10^{-4}$  are not reported in this table. For  $\text{SrTiO}_3$ , the Hamiltonian  $D_6$  to  $D_{28}$  parameters are the same as in Mattheiss' work.<sup>5</sup>

The Hamiltonian and overlap Bloch matrix elements between  $\chi_{\mu i \mathbf{k}}$  functions are evaluated by the analytical relations given by Michel-Calandini<sup>8</sup> for  $O_h^1$  and  $C_{4v}^1$  space groups, complemented to include  $A-A$  and  $A-B$  interactions.

The  $E_n(\mathbf{k})$  energies are computed in 13 824 equivalent points in the first Brillouin zone. The density of states and all related integrated functions, such as the joint density of states and the interband contribution of complex dielectric function  $\epsilon(E)$ , are deduced from electronic levels. The values of  $E_n(\mathbf{k})$  in the first Brillouin zone and DOS histograms are given on Figs. 5-7 for  $\text{SrTiO}_3$ ,  $\text{BaTiO}_3$ , and  $\text{KNbO}_3$ , when the parameters denoted  $D^*(A-B$  and  $A-O$  interactions) and  $D^{**}$  (part of the  $B-O$  interactions) are taken to be zero in the computations. The contribution of these additional parameters to the VB shape is discussed in the

next section.

#### IV. DENSITY OF STATES: THEORETICAL DETERMINATION AND XPS SPECTRA

##### A. Influence of symmetry in the DOS

XPS measurements are obtained for tetragonal  $\text{BaTiO}_3$  ( $D_{4h}^1$  space group) and orthorhombic  $\text{KNbO}_3$  ( $C_{2v}^{14}$  space group), while the band structures of Sec. III are given for the paraelectric phase. The problem is to estimate how far the cubic band schemes are distorted by the symmetry changes and if the comparison with the XPS results remains valuable. Both diagonal and off-diagonal matrix elements in Table II are affected by symmetry lowering. In the framework of our approximations, if the atomic ionic charges are kept constant, the changes in diagonal terms occur from Madelung potential variations reported in Table III. Lattice parameters and atomic displacements are taken from reference<sup>24</sup> for  $\text{BaTiO}_3$  and from Hewatt's work<sup>25</sup> for  $\text{KNbO}_3$ . The Madelung shifts induced by symmetry changes are very

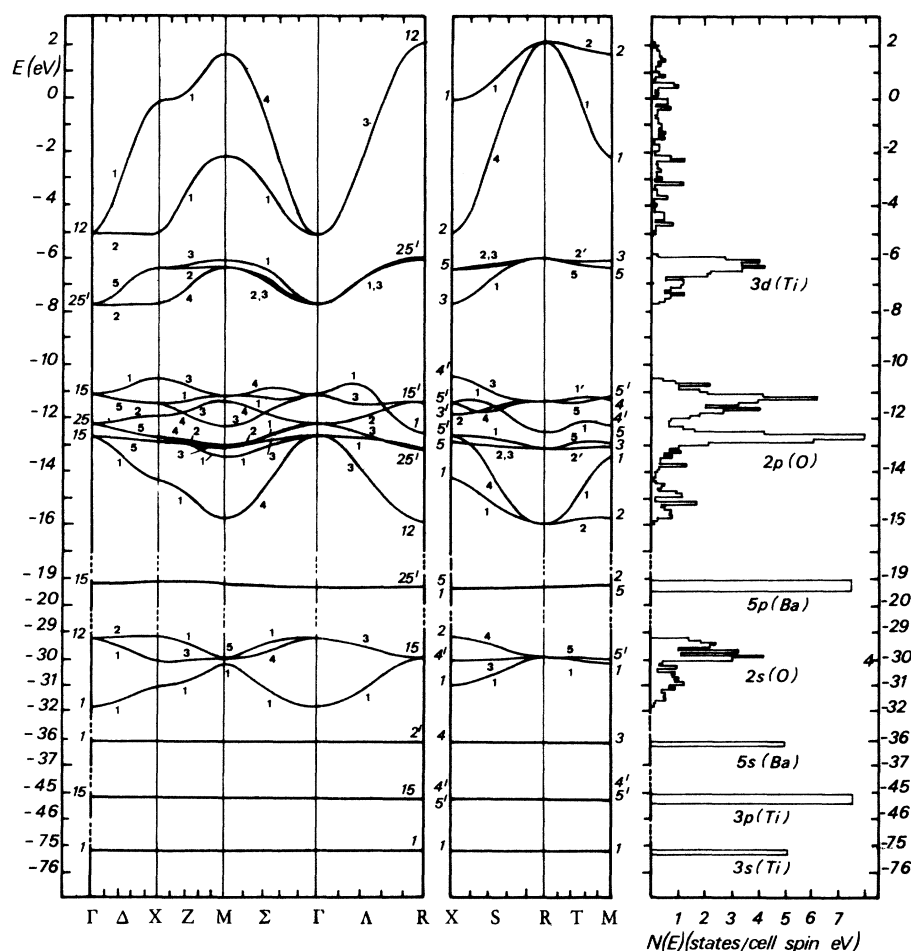


FIG. 6. Band-structure results and density of states (on the right-hand side) for  $\text{BaTiO}_3$ .

TABLE III. Madelung potentials at the various sites of  $ABO_3$  structure (in eV) for  $KNbO_3$  and  $BaTiO_3$ .

KNbO <sub>3</sub>			BaTiO <sub>3</sub>		
Sites	O <sub>h</sub> <sup>1</sup>	C <sub>2v</sub> <sup>14</sup>	Sites	O <sub>h</sub> <sup>1</sup>	D <sub>4h</sub> <sup>1</sup>
K <sup>+</sup>	-11.28	-11.27	Ba <sup>2+</sup>	-18.60	-18.58
Nb <sup>4+</sup>	-42.03	-41.90	Ti <sup>3+</sup>	-34.67	-34.72
O <sup>5/3-</sup>	20.54	20.60	O <sup>5/3-</sup>	18.78	18.89
	20.54	20.44		18.78	18.76
	20.54	20.44		18.78	18.76
K <sup>+</sup>	-12.07	-12.07	Ba <sup>2+</sup>	-19.39	-19.36
Nb <sup>5+</sup>	-51.90	-51.73	Ti <sup>4+</sup>	-44.54	-44.59
O <sup>2-</sup>	25.00	25.09	O <sup>2-</sup>	23.23	23.35
	25.00	24.87		23.23	23.23
	25.00	24.87		23.23	23.23

small compared to the variations upon the ionic charges. So, the  $O_h^1$  electronic levels are split or shifted by the off-diagonal parameter changes in the  $D_{4h}^1$  or  $C_{2v}^{14}$  symmetries. In short, however, if the calculated differences between the two phases are significant for the interpretation of transport and optical properties in  $BaTiO_3$  or  $KNbO_3$ , they remain less than the spectrometer resolution (0.55 eV) or perturbations induced by experimental conditions in XPS measurements. Indeed, when we compare the core positions in XPS data, we observe no significant changes in K and O inner photopeak positions in cubic  $KTaO_3$  (Ref. 29) and orthorhombic  $KNbO_3$  and in Ti-3p and O-2s states in cubic  $SrTiO_3$  (Ref. 3) and tetragonal  $BaTiO_3$ .

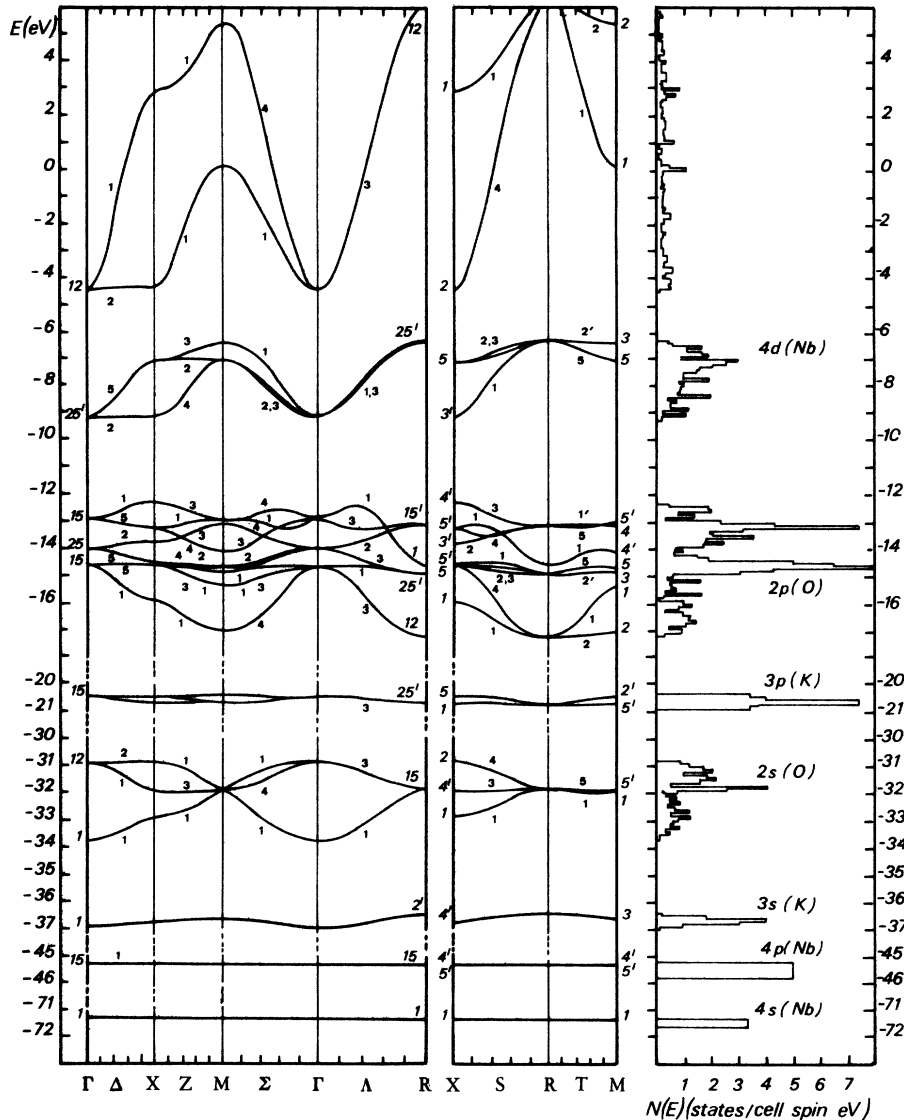


FIG. 7. Band-structure results and density of states (on the right-hand side) for  $KNbO_3$ .

### B. Introduction of the photoionization cross sections in the DOS

Let  $\sigma_i^\mu$  be the  $i$ th atomic subshell photoionization cross section of the  $\mu$  atom and  $P_{in}^\mu(\vec{k})$  the gross atomic population of the  $\chi_i^\mu$  orbital belonging to the  $\Phi_{n\vec{k}}$  orbital. According to Gelius,<sup>26</sup> the total cross section relative to  $E_n(\vec{k})$  can be expressed by:

$$\sigma_n(\vec{k}) = \sum_{\mu} \sum_i P_{in}^\mu(\vec{k}) \sigma_i^\mu. \quad (5)$$

For a given  $\vec{k}$ , the  $P_{in}^\mu(\vec{k})$  are computed by a Mulliken population analysis<sup>20</sup> and the  $\sigma_n(\vec{k})$  are determined for each  $E_n(\vec{k})$ . Then the corrected DOS is obtained according to the relation

$$N_c(E) = \frac{\Omega}{4\pi^3} \sum_n \int_{\vec{k}} d^3\vec{k} \sigma_n(\vec{k}) \delta(E_n(\vec{k}) - E). \quad (6)$$

(The usual DOS is obtained when  $\sigma_n(\vec{k})=1$ ), where  $\Omega$  stands for the volume of the unit cell. The atomic photoionization cross sections  $\sigma_i^\mu$  are taken from calculated tables.<sup>27</sup>

In Figs. 8 and 9, respectively, for BaTiO<sub>3</sub> and KNbO<sub>3</sub>, the corrected DOS including photoionization cross sections (curves c) are compared to the theoretical DOS (curves b) and to XPS valence bands (curves a). A background subtraction is applied on experimental spectra. This subtraction is such that the number of inelastically scattered electrons is taken to be proportional at any

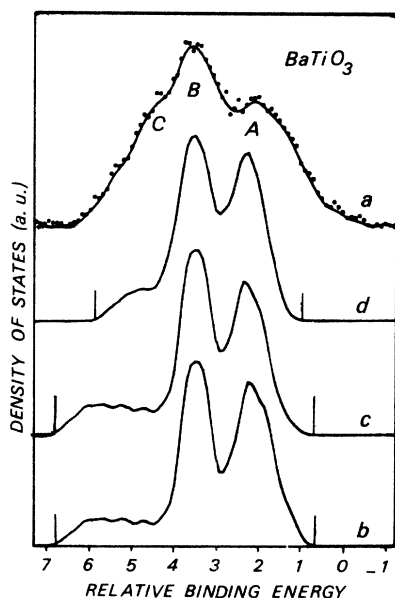


FIG. 8. Comparison between XPS valence-band spectrum of BaTiO<sub>3</sub> (curve a) and theoretical densities of states; (b) calculation corresponding to the band structure of Fig. 6; (c) introduction of photoionization cross-section; (d) as a comparison, density of states of SrTiO<sub>3</sub> corresponding to the band structure of Fig. 5.

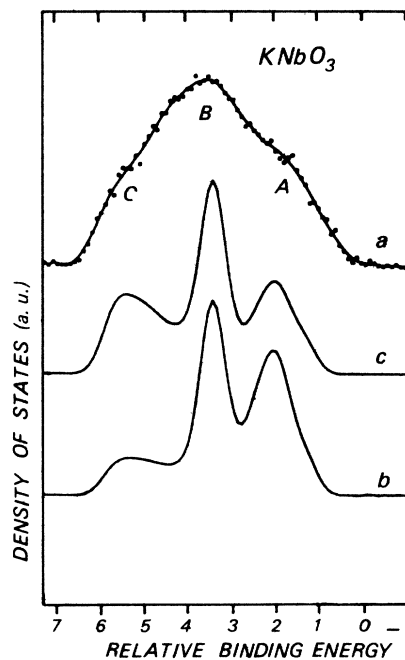


FIG. 9. Comparison between XPS valence-band spectrum of KNbO<sub>3</sub> (curve a) and theoretical densities of states; (b) calculation corresponding to the band structure of Fig. 7; (c) introduction of photoionization cross sections.

point to the integrated number of unscattered electrons of higher kinetic energy. In Figs. 8 and 9, the smoothed curves (a) are obtained from experimental points by a Fourier transform procedure which permits a better visualization of the VB structures. The DOS histograms are convoluted with a Gaussian of 0.55-eV full width at half-maximum (FWHM) taken to represent the spectrometer resolution function. In Fig. 8(d) the DOS of SrTiO<sub>3</sub> deduced from the band scheme of Fig. 6 is also reported.

The experimental VB of BaTiO<sub>3</sub> and KNbO<sub>3</sub> appear to be similar, with two well differentiated structures denoted A and B. An additional shoulder C can be distinguished at higher binding energies. The peak A, located about 1.5 eV below the VB edge can be related to nearly pure oxygen states such as  $^1\Gamma_{15}$ ,  $^1X_5$ ,  $R_{15}$ , while the peaks B and C arise from  $2p$ - $md$  mixed states. The energy difference between peaks A and B is correctly reproduced in the theoretical DOS. Introduction of photoionization cross sections induces very small changes in VB of BaTiO<sub>3</sub> since  $\sigma_{3d}^{Ti}$  and  $\sigma_{2p}^O$  are of the same order. For KNbO<sub>3</sub>, the intensity ratios of peak B to peak A and peak C to peak A are increased since  $\sigma_{4d}^{Nb} \approx 10\sigma_{2p}^O$ . The experimental band width is about 0.5 eV larger in KNbO<sub>3</sub> than in BaTiO<sub>3</sub>; this is related to the fact

that  $B$ - $O$  interactions are stronger for Nb than for Ti.

The contribution of  $D_{27}(pd\sigma)$  parameters is preponderant in the energies of  $R_{12}$ ,  $M_1$ ,  $X_1$ , and  $M_2$  type symmetry states, associated with peak  $C$  in the VB of Figs. 8 and 9. The  $D_{28}(pd\pi)$  integrals act on  $R_{25^*}$ ,  $M_5$ , and  $X_5$  level energies, related to peak  $B$ . Valence and conduction band widths vary with  $D_{27}$  and  $D_{28}$  Hamiltonian integrals values, with a stronger effect for the conduction band width.

In theoretical  $BaTiO_3$  DOS of Fig. 8, the structure  $C$  is shifted towards higher binding energies and the splitting between peak  $B$  and VB bottom ( $R_{12}$  state) is about 0.6 eV stronger in convoluted histogram (curve b) than in XPS data (curve a). Reverse effects are observed for the  $SrTiO_3$  DOS (curve d). In a first approximation, the  $BaTiO_3$  ( $pd\sigma$ ) value appears to be rather strong, while the  $SrTiO_3$  one is probably too weak.

Moreover oxygen-oxygen interaction terms contribute to the  $2p$  diagonal elements in overlap and Hamiltonian matrix relevant to  $2p-md$  mixed representations and modify the corresponding level energies. This fact is pictured by the DOS histogram of Fig. 6 for  $SrTiO_3$  and by the curve in Fig. 8: in this case the only difference with Mattheiss's computations<sup>5</sup> is the introduction of additional overlap elements, without variation of Hamiltonian matrix parameters. The intensity ratio of peaks  $A$  and  $B$  is reversed with regard to the adjusted DOS of reference.<sup>5</sup> We note that in this computation, the choice of the zero of energies at  $\Gamma_{15}$  level minimizes the effect of oxygen overlap elements on the location of states. Furthermore, if the oxygen-oxygen ( $sp\sigma$ ) interactions given by the  $D_{18}$  and  $D_{19}$  parameters are taken into account in this computation, the VB edge is an  $X'_4$  state instead of  $\Gamma_{15}$ , and the slope of the DOS near the VB edge becomes less important<sup>21</sup> than in curve d.

### C. Extended band structure and VB of $BaTiO_3$

The  $D^*$  and  $D^{**}$  parameters in Table II denote the interactions of  $A$  and  $B$  inner orbitals neglected in the band computations of part 3. The different contributions of these parameters to the VB shape are shown in Fig. 10 for  $BaTiO_3$ . Below the XPS density of states (curve 10a), the convoluted DOS histograms are plotted when only  $D^*$  (curve 10b),  $D^{**}$  (curve 10c), or both  $D^*$  and  $D^{**}$  parameters (curve 10d) are introduced into the Hamiltonian and overlap matrix in addition to the  $D_1$  to  $D_{28}$  elements.

Since the additional orbitals do not belong to the  $R_{12}$  representation, the bottom of the VB remains unchanged. The DOS near the valence-band edge located at  $X'_4$  is modified. The introduction of  $A$ - $O$

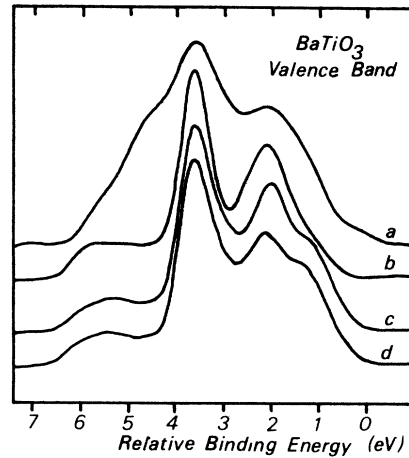


FIG. 10. Influence of different matrix elements interactions on the calculated density of states of  $BaTiO_3$ : (a) experimental; (b) with  $D^*$  parameters taken into account; (c) with  $D^{**}$  parameters taken into account; (d) with both  $D^*$  and  $D^{**}$  taken into account.

interactions ( $D_{34}^{**}$  to  $D_{38}^{**}$ ) shift the  ${}^1X'_4$  level upward by 0.4 eV, while additional  $B$ - $O$  parameters ( $D_{29}^*$  to  $D_{33}^*$ ) increase by the  ${}^1X'_4$  position by only 0.05 eV. However, the direct gap  ${}^1\Gamma_{15} - \Gamma_{25}$  is decreased by 0.8 eV under the repulsive effect of  $B(ms)$  and  $B(mp)$  orbitals at  $\Gamma_{15}$ , and the order the  $\Gamma_{15}$  and  $\Gamma_{25}$  levels can be inverted under the influence of  $(mp|2p)$  and  $(ms|2p)$  interactions ( $D_{32}^*$  and  $D_{33}^*$ ). The  $A$ - $B$  interactions ( $D_{39}^{**}$  to  $D_{46}^{**}$ ) remain always weak and do not induce notable modifications of the whole band scheme. The total VB width is increased by about 0.5 eV; the same effect, but a little stronger, is observed for  $KNbO_3$ .

## V. CONCLUSION

In the case of these perovskite compounds, XPS measurements of the valence bands is representative of the real initial DOS and consequently the comparison with theoretical band schemes is significant. The reasons are the following. First, the  $O$ - $2p$  valence shell, in the classical molecular-orbital description, is complete and the electronic configuration is  $3d^0$  or  $4d^0$ , thus insuring the absence of multiplet splitting phenomena in the final hole state after the photoemission. Second, charge transfer shake-up satellites are observed, mainly on the transition-metal photo-peaks of  $BaTiO_3$ , and  $KNbO_3$  in the same way as in  $SrTiO_3$ ,<sup>28</sup> but the energy separation between the main peak and the first satellite is always large enough to eliminate any interference with the observed valence band. Third, since the valence band is mainly of oxygen  $2p$  character, we do not think that relaxation phenomena could distort the

valence-band shape. The last point concerns the mean life of the photoionized states giving rise to the natural widths of the energy levels. These natural widths are not well known. They are certainly small. However, they induce always a broadening of the photopeaks. Thus, it seems reasonable to obtain slightly narrower peaks in theoretical DOS than in XPS spectra, even when the convolution by the spectrometer function is performed.

XPS valence bands of BaTiO<sub>3</sub>, KNbO<sub>3</sub>, and SrTiO<sub>3</sub> (Ref. 3, for example) reveal very similar structures: one main peak *B*, with one shoulder on each side. From the calculated band schemes, we can analyze the total valence band in the following way; the peak *A*, near the VB edge is formed by nearly pure oxygen states  $\Gamma_{15}$ ,  $R_{15}$ ,  $X_5$ , and  $M_5$ . The peak *B* is associated with  $X_5$  and  $M_3$  VB states, and the peak *C*, related to  $X_1$  and  $R_{12}$  states, depends mainly on the value of the *pd* $\sigma$  interaction. This analysis will be complemented by calculations of the energy distribution of *p* and *d* states in the VB.<sup>29</sup> On the whole, present theoretical results are in general agreement with XPS measurements, especially when

the inner orbitals of *A* and *B* cations are taken into account in computation. The *p-d* mixing remains small due to the large separation between  $2p$  and  $3d$  states, since the direct gap is about 3 eV in the three studied perovskites.

The tight-binding method is used here in a semi-empirical way with a parametrization of off-diagonal Hamiltonian matrix elements. The validity of the results are tested in regard to XPS and optical transition spectra and forbidden gap widths.

The intensity modulations induced by the photoionization cross sections are not very important in BaTiO<sub>3</sub> because  $\sigma_{2p}^O$  is of the same order as  $\sigma_{3d}^{Ti}$ . For KNbO<sub>3</sub>, the intensity ratios of peak *B* to peak *A* and peak *C* to peak *A* are increased coming from the  $4d$  states of the VB. The improvement goes in the right way by comparison to the XPS results.

#### ACKNOWLEDGMENTS

The authors are greatly indebted to Dr. G. Metrat and to Dr. F. Micheron for providing the high-quality single crystals of KNbO<sub>3</sub> and BaTiO<sub>3</sub> used in this work.

<sup>1</sup>R. Board, H. Weaver, and J. M. Honig, in *Electron Spectroscopy*, edited by D. A. Shirley (North-Holland, Amsterdam, 1972), p. 595.

<sup>2</sup>S. P. Kowalczyk, Ph.D. thesis (University of California, Berkeley, 1976) (unpublished).

<sup>3</sup>F. L. Batty, H. Hochst, and A. Goldmann, *Solid State Commun.* **19**, 269 (1976).

<sup>4</sup>A. H. Khan and A. J. Leyendecker, *Phys. Rev.* **135**, A-1321 (1964).

<sup>5</sup>L. F. Mattheiss, *Phys. Rev. B* **6**, 4718 (1972).

<sup>6</sup>T. F. Soules, E. J. Kelly, D. M. Vaught, and J. W. Richardson, *Phys. Rev. B* **6**, 1519 (1972).

<sup>7</sup>F. M. Michel-Calandini and G. Mesnard, *J. Phys. C* **6**, 1709 (1973).

<sup>8</sup>F. M. Michel-Calandini, Ph.D. thesis (Lyon, 1971) (unpublished).

<sup>9</sup>A. Linz, W. Belruss, and C. S. Naiman, *J. Electrochem. Soc.* **112**, 60C (1965).

<sup>10</sup>G. Metrat, Ph.D. thesis (Lyon, 1974) (unpublished); G. Metrat and A. Deguin, *Ferroelectrics* **13**, 527 (1975).

<sup>11</sup>E. Clementi, *J. Res. Develop.* **9**, 2 (1965).

<sup>12</sup>J. W. Richardson, M. J. Blackman, and J. E. Rano-chak, *J. Chem. Phys.* **58**, 3010 (1973).

<sup>13</sup>C. E. Moore, *Atomic Energy Levels*, Natl. Bur. Stand. Ref. Data Circ. No. 467 (U.S. GPO, Washington, D.C., 1949).

<sup>14</sup>H. Basch, A. Viste, and H. B. Gray, *Theor. Chim. Acta* **3**, 458 (1965).

<sup>15</sup>F. Herman and F. Skillman, *Atomic Structure Calculations* (Prentice-Hall, New York, 1963).

<sup>16</sup>G. B. Mann, *Atomic Structure Calculations* (unpublished).

<sup>17</sup>W. Van Gool and A. G. Piken, *J. Mater. Sci.* **4**, 95 (1969).

<sup>18</sup>M. Wolfsberg and L. Helmholz, *J. Chem. Phys.* **20**, 837 (1952).

<sup>19</sup>B. Jacquier, Ph.D. thesis (Lyon, France, 1976) (unpublished).

<sup>20</sup>R. S. Mulliken, *J. Chim. Phys.* **46**, 497 (1949).

<sup>21</sup>L. Castet and F. M. Michel-Calandini (unpublished).

<sup>22</sup>R. E. Watson, *Phys. Rev.* **111**, 1108 (1958).

<sup>23</sup>E. Clementi, D. L. Raimondi, and W. P. Reinhardt, *J. Chem. Phys.* **47**, 1300 (1967).

<sup>24</sup>F. Jona and G. Shirane, *Ferroelectric Crystals* (Pergamon, Oxford, 1962).

<sup>25</sup>A. W. Hewat, *J. Phys. C* **6**, 2559 (1973).

<sup>26</sup>U. Gelius, in *Electron Spectroscopy*, edited by D. A. Shirley (North-Holland, Amsterdam, 1972), p. 311.

<sup>27</sup>J. H. Scofield, *J. Electron Spectrosc. Relat. Phenom.* **8**, 129 (1976).

<sup>28</sup>K. S. Kim and N. Winograd, *Chem. Phys. Lett.* **31**, 312 (1975).

<sup>29</sup>P. Pertosa and F. M. Michel-Calandini (unpublished).